This is the peer-reviewed, final accepted version for American Mineralogist, published by the Mineralogical Society of America.
The published version is subject to change. Cite as Authors (Year) Title. American Mineralogist, in press.
DOI: https://doi.org/10.2138/am-2023-9062. http://www.minsocam.org/

Revision 2

Jarosite formation in Permian-Triassic strata at Xiakou (South China): Implications for jarosite precipitation from H_2S upwelling on Mars

Hanlie Hong[1*], Chen Liu[1], Thomas J. Algeo[1,2], Elizabeth B. Rampe[3]

[1]*State Key Laboratory of Biogeology and Environmental Geology, China University of Geosciences, Wuhan 430074, China*

[2]*Department of Geosciences, University of Cincinnati, Cincinnati, OH 45221-0013, USA*

[3]*Astromaterials Research and Exploration Science Division, NASA Johnson Space Center, Houston, TX 77058, USA*

ABSTRACT

The source of sulfuric acid and associated aqueous alteration of ancient Martian sedimentary rocks remain under debate in the context of divergent models of jarosite formation. Here, we report the formation of sulfates including jarosite in K-bentonites within shallow-water facies of the Permian–Triassic (P-T) transition at Xiakou in South China. In these strata, jarosite is dispersed in the clay matrix or forms aggregates in pore spaces, has a euhedral morphology, and co-exists with variably ^{34}S-depleted paragenetic gypsum and bassanite ($\delta^{34}S$ = –37.23‰ to +3.20‰ VCDT). Subaqueous alteration of volcanic tuffs concurrently with oxidation of upwelled, biogenically sourced H_2S is the process of jarosite formation in the Xiakou K-bentonites. This mechanism of jarosite precipitation and stability over geological time challenges the long-held view of acidic, water-limited conditions leading to iron(III) sulfate precipitation and would be consistent with possible microbial or nanobial life on early Mars.

Keywords: Tuff; K-bentonite; smectite; jarosite; sulfates; microbial reduction

---

*Email: honghl8311@aliyun.com (Hanlie Hong)

Always consult and cite the final, published document. See http:/www.minsocam.org or GeoscienceWorld

This is the peer-reviewed, final accepted version for American Mineralogist, published by the Mineralogical Society of America.
The published version is subject to change. Cite as Authors (Year) Title. American Mineralogist, in press.
DOI: https://doi.org/10.2138/am-2023-9062. http://www.minsocam.org/

INTRODUCTION

Global mineralogical observations of Mars via orbital reflectance spectroscopy have revealed an apparent evolution in the secondary mineral assemblage during the earliest history of the planet (Bibring et al., 2006). The Noachian-aged (4.1-3.7 Ga) stratigraphic units are dominated by Fe/Mg-smectites, with minor amounts of Ca-sulfates and Fe-oxides, whereas the younger Hesperian-aged (3.7-3.1 Ga) units more commonly consist of Mg/Ca/Fe-sulfates, with fewer detections of clay minerals, hematite, and hydrated silica (Ehlmann and Edwards, 2014). The widespread clay minerals on Mars record clear evidence for water-rich surface and near-surface environments in Mars' past, since smectite often forms by supergene weathering under relatively warm and humid climate conditions on Earth (Sulieman et al., 2020; Saricaoglu et al., 2021; Hong et al., 2023). After extensive formation of phyllosilicates in the Noachian era, the abundance of sulfates, especially jarosite, in Hesperian-aged sediments is thought to reflect a substantial change in surface-water chemistry from near-neutral to acidic and saline owing to a dramatic change in the climate of Mars (Bibring et al., 2006; Hurowitz et al., 2017; Poulet et al., 2005).

Jarosite on Earth often occurs in arid, acidic, sulfate-rich weathering systems linked to supergene weathering of sulfides (Bauer and Velde, 1997) and in fumaroles and acidic-saline gr—oundwaters associated with lake systems (Benison, 2006). It is thermodynamically stable in a narrow pH range (~3-5) and is considered to be diagnostic of sulfuric acid oxidation and water-limited conditions (Potter-McIntyre and McCollom, 2018; Yoshida et al., 2018). Thus, the formation processes and environmental conditions experienced by jarosite-bearing Martian rocks have been inferred largely from the presence of jarosite.

In addition to orbital detection, jarosite has been identified in situ by the *Opportunity* rover on the Meridiani Planum and the *Curiosity* rover in Gale crater. Compositional data and images from the ground allow for more detailed interpretations of environments that led to jarosite formation. The evaporitic sandstones of the Burns Formation on the Meridiani Planum contain up to 10 wt.% jarosite and are thought to have been reworked by eolian and subaqueous processes and further altered by early and late diagenesis, during which jarosite may have formed as an evaporative cement following groundwater recharge (McLennan et al., 2005). Many alternate hypotheses to explain the jarosite have been proposed, including water-limited aqueous alteration followed by extreme aridity to preserve this mineral (Elwood Madden et al., 2004), aqueous

Always consult and cite the final, published document. See http:/www.minsocam.org or GeoscienceWorld

oxidation of hydrothermal sulfides (Zolotov and Shock, 2005), fumarolic SO_2-bearing vapor alteration of volcanic ash (McCollom and Hynek, 2005), and sediment reworking in conjunction with acid-sulfate weathering of massive ice deposits (Niles and Michalski, 2009). Jarosite has been detected in early Hesperian-aged, smectite-bearing, and typically Ca-sulfate-bearing fluvio-lacustrine deposits in Gale crater in abundances up to ~3 wt.% (Rampe et al., 2017; 2020). Hypotheses for jarosite precipitation include early or late diagenetic alteration of sulfides (Hurowitz et al., 2017; Rampe et al., 2017). K-Ar dating of one drill powder by the Sample Analysis at Mars (SAM) instrument yielded a relatively young age of 2.12±0.36 Ga for the jarosite, providing further evidence of a late diagenetic origin for jarosite in Gale crater (Martin et al., 2017).

Characterizing jarosite-bearing Mars-analog environments on Earth can help us further understand the mechanisms by which jarosite on Mars may have been precipitated and preserved. Here, we report the formation of jarosite and Ca-sulfate in altered volcanic tuffs within shallow-water settings of the Permian–Triassic (P-T) transition at Xiakou, South China. Our observations show that subaqueous weathering of volcanic materials associated with oxidation of upwelling biogenic H_2S from below the chemocline yielded jarosite-bearing smectitic mudstones. The striking mineralogical and depositional similarities to Martian deposits make the formation model and environmental conditions of the Xiakou K-bentonites a reasonable terrestrial analog for fine-grained sediments of the Red Planet, thus providing new insights into the geological processes that precipitated jarosite in Martian rocks.

SAMPLING AND METHODS

Sampling

The Xiakou stratal succession (31°6′51″N, 110°48′13″E) comprises the Permian Chihsian to Lower Triassic Smithian stages. The depositional setting of the Xiakou region was a distal carbonate ramp, characterized by shallow to somewhat deeper water, open-shelf facies during the Permian–Triassic (P-T) transition (Pei et al., 2020). The 1.8-m-thick P-T transition interval consists of gray mudstones and pale-yellow marls, interbedded with eight thin layers (each 1-4 cm thick) of altered volcanic tuff (K-bentonite) (Fig. 1). Most tuff beds in the Xiakou section have sharp contacts with underlying and overlying background deposits, indicating limited vertical

sediment mixing. The profile was first cleaned by removing loose surficial materials prior to sampling. Bulk samples, each weighing ~500 g, were collected from each ash layer (*N*=8) and its host rock (*N*=15) from the profile. The soft volcanic ash was excavated using a small trowel from between layers of the hard host rock.

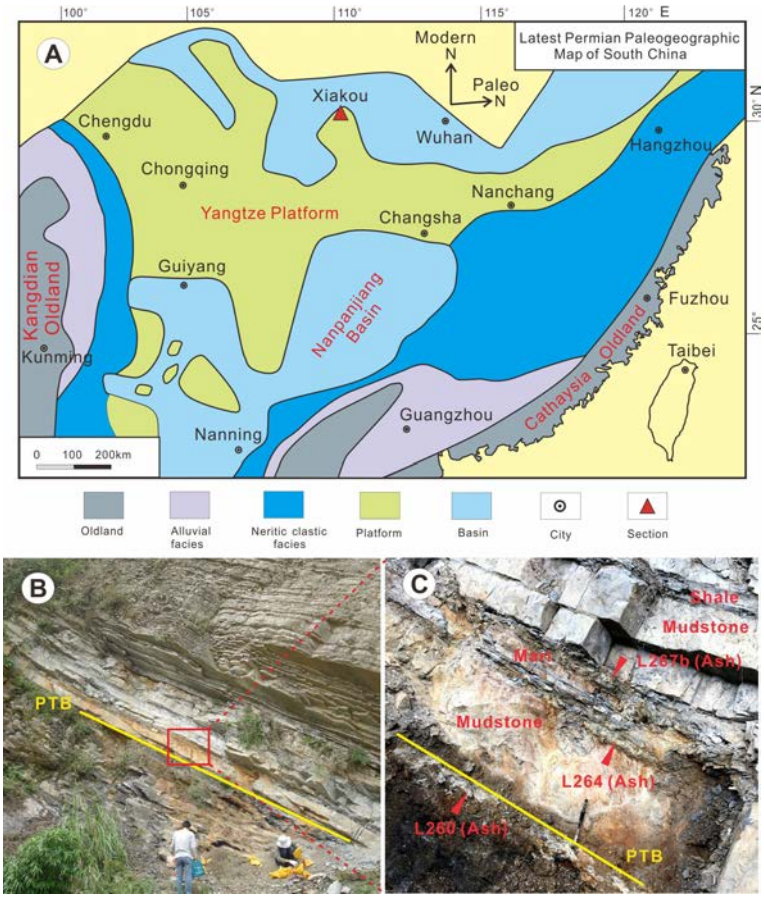

Fig. 1 Location and lithology of the Xiakou section. (A) Paleographic map of South China during the Permian-Triassic transition (~252 Ma) (modified from Algeo et al. (2013); (B) The full Xiakou P-T transition sequence; (C) A close-up photograph showing interbedding of tuff beds with marl and mudstone (pen length 15 cm).

X-ray diffraction（XRD）

Bulk samples were dried in an electric dry oven at 60 ◦C overnight and then ground to powder. The clay fraction (< 2 μm) was extracted using the sedimentation method. The relative proportions in the purified clay samples were determined by fitting the XRD spectra of glycolated oriented clay samples using the NEWMOD II program (Reynolds and Reynolds, 1996). The oriented clay samples were prepared by pipetting the clay suspension onto glass slides, and the glycolated treatment was performed by treating the air-dried oriented samples with ethylene glycol vapor in a

desiccator at 65 °C for 4 h. Mineral compositions of the bulk samples were obtained according to the XRD results of non-oriented powdered samples. An internal standard (zincite, ZnO) X-ray diffraction method was used to estimate the abundances of mineral phases in bulk samples. These bulk samples were prepared by mounting the powders into sample holders using a back-press technique to yield non-oriented powdered samples. X-ray diffraction analysis was undertaken on a Panalytical X'Pert PRO DY2198 diffractometer at 35 kV voltage and 30 mA current with Ni-filtered $Cu_{K\alpha}$ radiation. The XRD patterns were collected from 3° to 30° for oriented clay samples and from 3° to 65° 2θ for bulk samples at a scan rate of 4° 2θ/min, which were performed in three times respectively. The mineral intensity factor (MIF) values of these minerals were first measured at routine experimental conditions, and the content (wt.%) of a non-clay mineral in the bulk sample was calculated by the formula: $\%X=(I_X \cdot M_S \cdot 100)/(I_S \cdot MIF \cdot M)$, where M_X and M are the masses of mineral X and the sample to which standard is added, I_X and I_S are the intensities of reflections belonging to X and S in a mixture of a sample with the standard, and %X is the actual amount of the mineral in a sample without the standard (Środoń et al., 2001). The content of total clay minerals in a bulk sample was estimated from the sum of measured minerals departing from 100%. The characteristic peaks for mineral identification include 3.11 Å (jarosite), 2.68 Å (gypsum), 3.00 Å (bassanite), 2.70 Å (pyrite), 3.03 Å (calcite), 2.90 Å (ankerite), 2.88 Å (dolomite), 4.26 Å (quartz), 3.19 Å (plagioclase), and 3.22 Å (orthoclase). The mineral intensity factor values for these minerals are 0.512 (jarosite), 0.302 (gypsum), 0.456 (bassanite), 0.94 (pyrite), 1.07 (calcite), 0.92 (ankerite), 0.82 (dolomite), 0.29 (quartz), 0.71 (plagioclase), and 0.45 (orthoclase). The relative error of measurement of mineral phase content is generally <15%.

Scanning electron microscope（SEM）

Small blocks of ash samples were prepared, epoxied with resin, polished to produce a smooth surface, and subsequently carbon-coated. Microscopic observation was performed on a SUPRA 55 thermal field emission scanning electron microscope (FESEM) equipped an energy-dispersive spectrometer (EDS) and operated at 20 kV accelerating voltage and a beam current in the range of 1–3 nA. The chemical compositions of mineral particles were determined using the EDS system, with backscattered electron imaging used to analyze finer-grained particles.

High-resolution transmission electron microscopy（HRTEM）

HRTEM observations were undertaken on a FEI TECNAI G2 S-TWIN field-emission HRTEM equipped with an EDAX solid-state EDX detector and a Gatan 830 charge-coupled device (CCD) camera system. The instrument was operated at an accelerating voltage of 200 kV, with a point-to-point resolution of 0.24 nm and a line resolution of 0.14 nm. The area selected for electron diffraction was usually at the relatively thin edge of crystals, and the diffraction patterns were analyzed using the Digital Micrograph software version 3.9 (Gatan Ltd.) and compared to standard diffraction patterns of jarosite (PDF 71–1777; Formula of $K(Fe_3(SO_4)_2(OH)_6$, rhombohedral R-3m symmetry, and cell parameters: $a_0 = b_0 = 7.315$ Å, $c_0 = 17.224$ Å).

Major- and trace-element analyses

The major element compositions of the samples were measured using X-ray fluorescence (XRF) spectroscopy. Samples were prepared as fused pellets using dilithium tetraborate-polyvinyl alcohol. The measurement of major element compositions was undertaken on a Shimadzu XRF-1800 sequential XRF spectrometer with a rhodium tube at a 2.5 kW generator. The detection limit for major elements was ~0.01 wt%, and the relative standard deviation was <1%. Trace element analysis of whole-rock sample was conducted on an Agilent 7700e ICP-MS. The samples were digested in a mixed solution of hydrofluoric acid and nitric acid. The relative standard deviation was ~4% for REEs and 5–10% for other trace elements.

$^{34}S_{CaSO4}$ composition analysis

Gypsum and bassanite grains (usually 30-200 μm) were glued to a sample target with 50 grains per sample. In-situ sulfur isotope analysis of gypsum and bassanite was conducted on a Neptune Plus multireceiver inductively coupled plasma mass spectrometer (MC-CIP-MS) at mass resolving power (Rpower(5, 95%)) of 4996 equipped with an NWR FemtoUC femtosecond system. In the laser system, helium was used as the carrier gas for the ablation cell and was mixed with argon (makeup gas) after the ablation cell. The single spot ablation mode was used with a spot size of 40 μm, a slow pulse frequency of 4 Hz, and a laser fluence of ~2.5 J/cm^2. The $^{34}S/^{32}S$ ratio of the standards and samples were directly analyzed using static mode, with the total acquisition time for each measurement being approximately 52 s. $\delta^{32}S$ and $\delta^{34}S$ values were calculated using the

This is the peer-reviewed, final accepted version for American Mineralogist, published by the Mineralogical Society of America.
The published version is subject to change. Cite as Authors (Year) Title. American Mineralogist, in press.
DOI: https://doi.org/10.2138/am-2023-9062. http://www.minsocam.org/

calibration method of standard-sample bracketing (SSB) to avoid matrix effects. The natural barite standard GTS ($\delta^{34}S_{V\text{-}CDT}$ = +4.7±0.4‰) was used as a reference material for calibration of isotopic results. The in-house natural barite standards YF-1 ($\delta^{34}S_{V\text{-}CDT}$ = +18.5±0.7‰) and YF-2 ($\delta^{34}S_{V\text{-}CDT}$ = +18.1±0.4‰) were analyzed repeatedly as unknown samples to verify the accuracy of the calibration method (Fu et al., 2017). The final $\delta^{34}S$ value of each sample was the average of 15 to 50 point analyses, with a relative standard deviation usually better than 0.7‰.

RESULTS

Mineral compositions of the Xiakou sediments

X-ray diffraction evidence shows that jarosite, gypsum, and bassanite are present as minor components in K-bentonites and only occasionally in their enclosing host mudstones (Fig. 2); Table 1). The mineral compositions of the tuff beds are dominantly clay minerals and minor quartz, plagioclase, jarosite, gypsum, bassanite, and pyrite, with trace amounts of calcite and ankerite in some beds (Fig. 3; Table 2). The mudstones consist dominantly of clay minerals, quartz, and plagioclase, with minor pyrite and occasionally jarosite and gypsum, while the marls contain mainly calcite, ankerite, clay minerals, and minor amounts of quartz, plagioclase, and pyrite. Jarosite exhibits an intimate association with gypsum. Clay phases in the tuffs are dominantly mixed-layer illite/smectite (I/S) clays, whereas those in the mudstones and marls consist mainly of illite and minor chlorite, with I/S present only in the lower part of the profile (Table 1).

Always consult and cite the final, published document. See http:/www.minsocam.org or GeoscienceWorld

This is the peer-reviewed, final accepted version for American Mineralogist, published by the Mineralogical Society of America.
The published version is subject to change. Cite as Authors (Year) Title. American Mineralogist, in press.
DOI: https://doi.org/10.2138/am-2023-9062. http://www.minsocam.org/

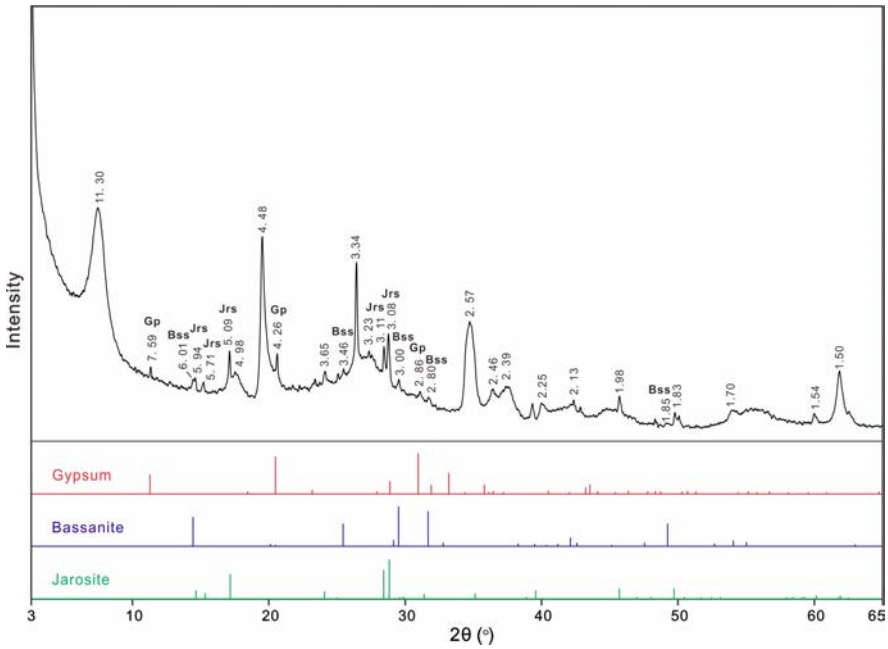

Fig. 2. Determination of jarosite (Jrs), gypsum (Gp), and bassanite (Bss) by XRD analysis of representative whole-rock tuff sample (L255).

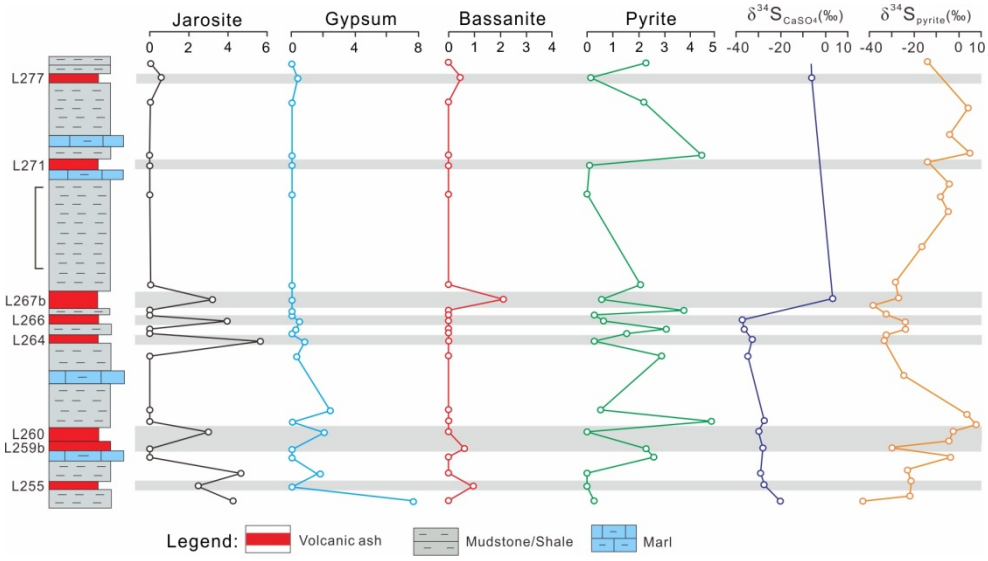

Fig. 3 Sulfate content and sulfur isotopic composition of Xiakou profile. (The scale bar is 30 cm in length; $\delta^{34}S_{pyrite}$ curve adapted from Shen et al. (2013))

Occurrence of jarosite in Xiakou tuffs

Back-scattered electron (BSE) microscopic observations and elemental mapping by SEM show that jarosite occurs both dispersed through the clay matrix and as aggregates in small pore spaces, rather than coating pyrite grains (Figs. 4A-D and 5). HRTEM observations show that jarosite exhibits both euhedral hexagonal and pseudo-cubic morphologies, with particle sizes

mainly of 150-400 nm and 50-150 nm, respectively. Both hexagonal and pseudo-cubic crystals display a uniform diffraction

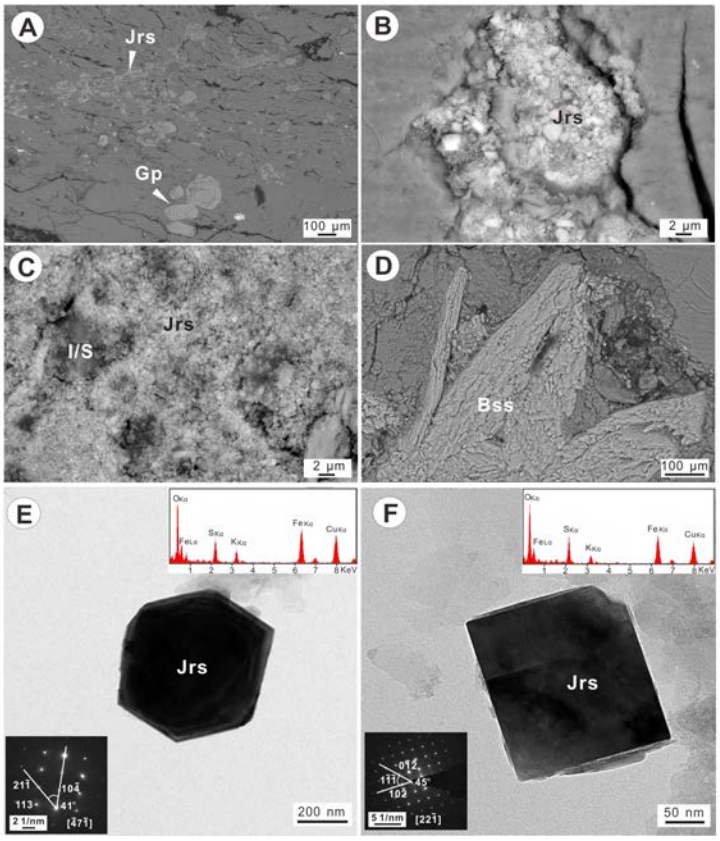

Fig. 4 Microscopic observations of authigenic minerals in the Xiakou tuff. (A) Jarosite nanoparticles associated with euhedral gypsum crystals (BSE); (B) Aggregated jarosite in a pocket within clay matrix (BSE); (C) Enlarged view of jarosite showing fine-grained morphology on clay flake substrate (secondary electron image); (D) Bassanite in subhedral crystals with orientation along the cleavage directions of gypsum showing its formation from dehydration of a gypsum precursor (BSE); Hexagonal (E) and pseudo-cubic (F) crystal habits of jarosite with electron diffraction patterns and energy-dispersive spectroscopy (EDS) spectra by HRTEM observation. (Jrs: jarosite; Gp: gypsum; I/S: mixed-layer illite/smectite; Bss: bassanite; BSE: back-scattered electron).

pattern compatible with the trigonal system of jarosite (R-3m), and the chemical composition resembles that of typical jarosite, *i.e.*, $KFe_3^{+3}(SO_4)_2(OH)_6$, as confirmed by EDS data (Fig. 4E, F).

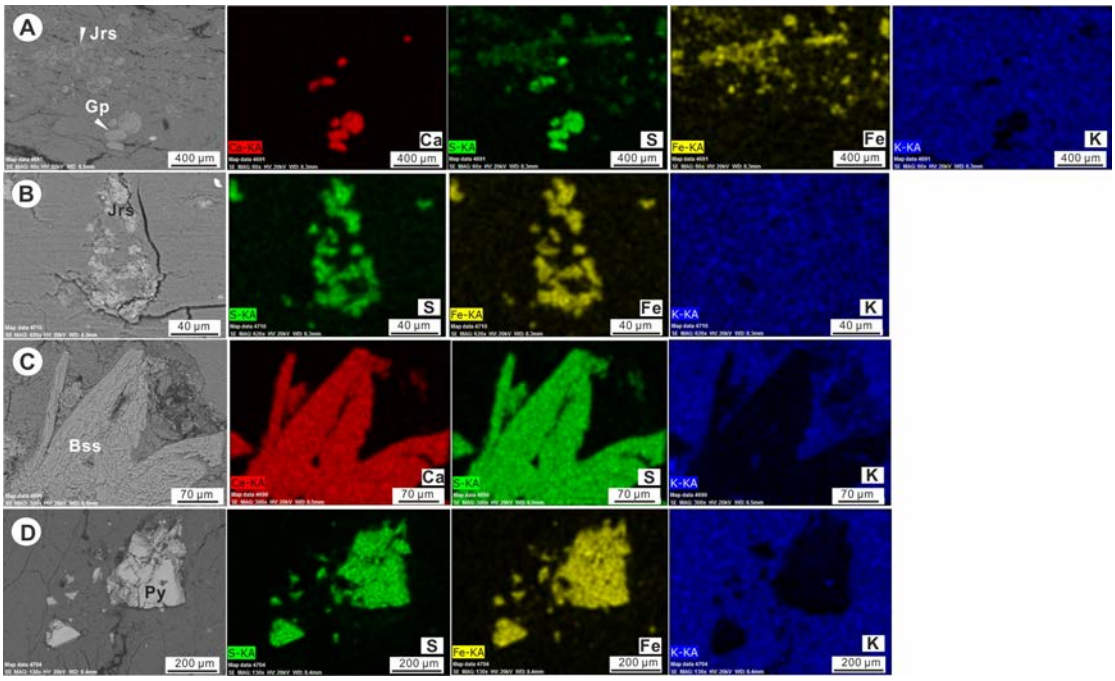

Fig. 5 Elemental mapping for jarosite and co-existing sulfates in the Xiakou K-bentonite. Overlapping distributions of (A) Ca and S indicate probable gypsum, and S, Fe, and K indicate dispersed jarosite; (B) S, Fe, and K reveal jarosite in a pocket-like space; (C) Ca and S indicate bassanite, supported by its crystal morphology; and (D) S and Fe indicate pyrite (Py).

Gypsum, which occurs in pore spaces of the clay matrix as euhedral, micrometer-sized (< 30 to 200 μm), isolated prismatic crystals or intergrown crystals (Figs. 4A and 5). Bassanite occurs in aggregates in pore spaces, where fine-grained (2 to 5 μm) crystals display a subhedral elongated prismatic shape typically oriented along a good cleavage direction {010} or the distinct cleavage planes of gypsum {100} and {011} (Figs. 4D and 5). Pyrite is widely present in the tuff beds and background sediments. It displays euhedral cubic and octahedral and, sometimes, irregular morphologies, being mainly 10-40 μm in size (Fig. 5D).

Geochemical compositions of the Xiakou sediments

The Xiakou tuffs have generally compatible major element compositions with relatively less variation between samples from different layers, consisting of mainly SiO_2, Al_2O_3, and K_2O (Table S1). The contents of SiO_2, Al_2O_3, and K_2O of the tuff samples ranged from 48.22 to 57.82%, 16.32 to 25.49%, and 4.49 to 6.18%, respectively. TiO_2 content is generally low (0.355–0.854%). The Fe_2O_3(t) content changed significantly from 1.33 to 5.92%, consistent with their varied mineral abundances of jarosite and pyrite. CaO ranged greatly from 0.91 to 4.67%, corresponding to

changes mainly in sulfate and carbonate contents. The tuff samples have relatively low and quite uniform MgO content (2.43–3.69%) compared to those of adjacent normal background sediments. Na_2O content is low (0.07 to 0.58%), with the single exception of sample L267b (1.04%) due to the presence of much more plagioclase. LOI values changed in a narrow range of 6.59 to 11.92%, consistent with the predominance of clay minerals determined by XRD analysis. Results of trace element and rare earth element analyses are reported in Table S2. Plots of TiO_2 versus Al_2O_3 and Zr/TiO_2 versus Nb/Y of the Xiakou tuffs show that the tuffs have felsic-intermediate source rocks (Fig. S1).

$\delta^{34}S$ values of sulfates in the Xiakou sediments

The $\delta^{34}S$ of gypsum and bassanite (n.b., jarosite was not measured due to small particle size) in the lower part of the profile ranges from –37.23 to –21.80‰ (Table 2), which is markedly lower than that of contemporaneous seawater sulfate of (~+15 to +25‰) (Kampschulte and Strauss, 2004) or magmatic sulfur (~0‰) (Marini et al., 2011). For some relatively larger grains, $\delta^{34}S$ value showed zoned distribution from the center to margin of the crystals. For example, the zoned $\delta^{34}S$ value of Sample L255 (tuff) increases from -30.74 to -24.88 and to -19.38‰, while that of L277 (mudstone) decreases from -15.12 to -20.11‰ (Table 3), suggesting the evolution of porewater with diagenesis.

DISCUSSION

Precipitation of sulfates in the Xiakou tuffs

Weathering of tuffs can occur quickly in syndepositional to early diagenetic environments, and the dissolved Si and Al released by dissolution of volcanic materials can lead to oversaturation of sediment porewater with respect to smectite (Christidis, 1998). In addition to the Si and Al incorporated by neoformed smectite, excess silicon can form Si-rich phases such as quartz, opal-CT, mordenite, and plagioclase or leach away. Authigenic smectite is usually converted to mixed-layer I/S via K-incorporation in the burial diagenetic environment, depending on burial temperatures and potassium availability (Somelar et al., 2010). The tuff beds in the Xiakou profile contain dominantly I/S clays, with minor plagioclase, quartz, carbonates, and sulfides, and variation in the smectite layer content of the I/S clays between tuff beds is likely attributable to

differences in parent-rock composition (Table 1; Fig. S1). This relationship is also reflected by relatively larger amounts of plagioclase, quartz, jarosite, and gypsum in the tuff beds having intermediate source rocks compared to those with felsic source magmas.

Microscopic observations showed that there is no evidence of potential precursor ferrous phases such as schwertmannite for formation of jarosite (Fig. 4A-C), suggesting that jarosite is unlikely to have formed via alteration of reduced Fe-minerals. In particular, the euhedral crystals of jarosite indicate that their precipitation took place directly from sediment porewaters under relatively slow precipitation kinetics, and that the two distinct morphologies of jarosite probably reflect two periods of formation under slightly different conditions (Fig. 4A-F). The disseminated and pocket-like occurrences of jarosite, especially on flakey clay substrates (Fig. 4C), suggest that it formed during the post-depositional to early diagenetic stages, prior to obvious compaction of the sediment.

The euhedral, isolated or intergrown crystals of gypsum in pore spaces of the Xiakou tuffs exhibit closely association with jarosite, indicative of initial precipitation from porewater (Figs. 4A and 5). The precipitation of gypsum likely took place before significant sediment compaction, concurrent with or slightly later than jarosite formation. Also, the large size of single crystals and crystal clusters suggests precipitation of gypsum by relatively slow growth in moderately supersaturated porewaters. In shape and size, the bassanite aggregates resemble those of gypsum crystals and clusters (Figs. 4D and 5), indicating its formation via dehydration of gypsum precursors. Transformation of gypsum to bassanite occurs under water-poor, high-temperature conditions and/or in high-salinity brines, as commonly encountered in the burial diagenetic environment (Hoareau et al., 2011). This transformation was facilitated by the nature of the Xiakou sedimentary environment, which was a moderately deep-water setting characterized by elevated salinity, oxygen depletion, and euxinia, as determined from sedimentary microfacies investigation (Pei et al., 2020). The paragenetic association of jarosite and gypsum in the clay matrix indicates concurrent formation of these minerals, both being related to the presence of sulfuric acid. The basanite originated via dehydration of gypsum and is expected to have inherited its sulfur source. The presence of pyrite is largely confined to void spaces, indicating that it formed during late diagenesis after the sediments had undergone a certain degree of compaction.

Formation of jarosite during alteration of tuff by upwelled H_2S

The source(s) of sulfur in the Xiakou profile can be inferred from the S-isotopic compositions of the constituent minerals. Although tuff particles often contain certain amounts of acid volatiles (e.g., SO_2, HF, and HCl) due to adsorption of volcanic aerosols (Cronin et al., 2014), the markedly lower $\delta^{34}S$ values of gypsum and bassanite in the Xiakou sediments (Table 2) exclude its source of seawater sulfate (Kampschulte and Strauss, 2004) or magmatic sulfur (Marini et al., 2011). Gypsum from organic-rich marine sediments has been considered as a marine atmospheric H_2S proxy, and the Xiakou sulfates with notably light isotopic compositions are characteristic of sulfur sourced from sulfate-reducing bacteria in the underlying sediments. Sulfate-reducing bacteria (e.g., *Desulfovibrio desulfuricans*) enrich metabolically produced H_2S in ^{32}S, resulting in $\delta^{34}S$ values as low as –46‰ (Kaplan and Ritterberg, 1964). The highly ^{34}S-depleted sulfates ($\delta^{34}S$ = –37.23 to –21.80‰) in the lower profile were likely derived from sulfate-reducing bacteria, taking into consideration the organic matter-rich underlying deposits (Pei et al., 2020; Shen et al., 2013) and the notably higher $\delta^{34}S$ values (–6.62 to +3.20‰) in the upper profile (L267b, L277). In particular, some larger crystals of gypsum exhibit zoned distribution of $\delta^{34}S$, increasing gradually from the center to margin of gypsum crystals in tuffs, while showing the opposite trend for gypsum in the adjacent mudstone, indicative of evolution of porewater chemistry in diagenesis. The $\delta^{34}S$ of pyrite fluctuates between +5% and −30% within the Xiakou profile (Fig. 3; Table 2). Heavier $\delta^{34}S$ values indicate a dominantly diagenetic origin of pyrite, whereas lighter values reflect a syngenetic origin from a euxinic water column (Shen et al., 2013; Lei et al., 2017).

The concurrent formation of jarosite, gypsum, and bassanite required acidic conditions, high salinity, and sources of K^+, Fe^{3+}, and SO_4^{2-} ions. Most the tuff beds in the Xiakou section show a sharp boundary with their enclosing deposits, indicating limited mixing with the normal background sediments, and the highly acidic porewater needed to precipitate sulfates is primarily derived from upwelling of H_2S accompanying sedimentation of volcanic tuffs. The deposition of the volcanic tuffs simultaneously introduced the flux of atmospheric O_2 and resulted in the formation of sulfuric acid ($H_2S + 2O_2 \rightarrow SO_4^{2+} + 2H^+$) (Fig. 6). The existence of acidic porewaters at Xiakou is also confirmed by the distinct crystallographic morphology of authigenic anatase, which has an acute tetragonal-bipyramidal habit in the tuffs (Hong et al., 2022), similar to that of anatase formed in the Verkhnekamskoe salt deposits at a pH of 4.7-5.9 (Chaikovskiy et al., 2019).

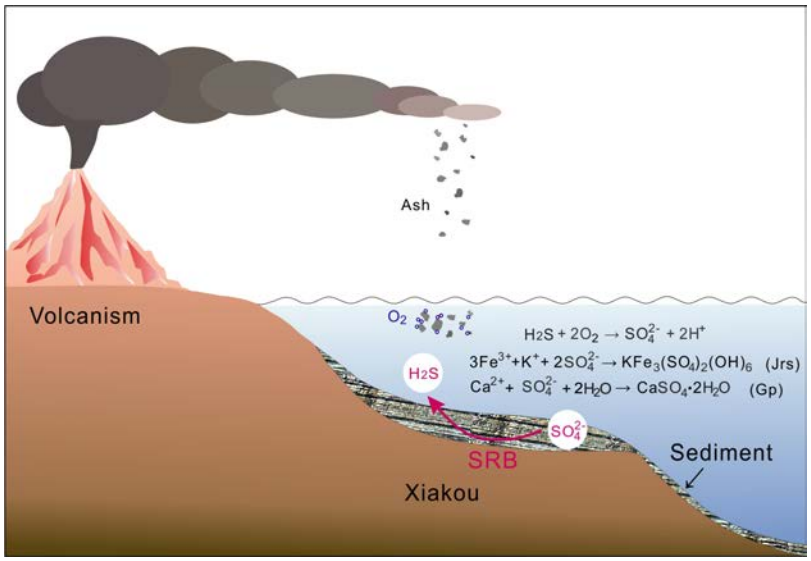

Fig. 5 Jarosite formation due to volcanic tuff deposition in combination with upwelling of H_2S produced by sulfate-reducing bacteria (SRB). (Jrs- jarosite; Gp- gypsum).

Potassium is a highly soluble component of volcanic glass that is almost completely leached from tuffs during early diagenesis (De La Fuente et al., 2002). However, diffusive loss of K^+ and other leached cations (e.g., Ca^{2+}, Mg^{2+}, Fe^{2+}) was low due to (1) the low porosity and permeability of the mudstones and marls enclosing the tuff layers at Xiakou, and (2) the mineralogy of the host marine sediments, which consists dominantly of illite and carbonates, yielding a porewater cation assemblage similar to that of the tuffs. These factors led to retention of leached cations including K^+ in the porewater of the tuffs and, thus, ultimately promoted the precipitation of jarosite.

The host sediment at Xiakou contains substantial Fe in the form of ankerite precipitated from ferruginous seawater under slightly reducing conditions (Table 2), with incorporation of Fe^{2+} into ankerite as a substituent for Mg^{2+}. However, iron in silicates tends to be released as Fe^{3+} during alteration of volcanic materials, and the formation of jarosite is most likely attributed to very local changes in chemistry, redox conditions, and element concentrations in the traps of sediments. As confirmed by jarosite formation in a silicic chalk elsewhere, weathering of dispersed pyrite and glauconite in the calcareous material led to the local precipitation of jarosite (Bauer and Velde, 1997). The absence of Fe(III)-oxide phases in the Xiakou tuffs is not only attributed to the relatively Fe-poor intermediate-felsic source rocks but also to good preservation of jarosite in the

low-pH environment, since decomposition of jarosite often produces iron oxides (Elwood Madden et al., 2012). Contrarily, weathering of Fe-rich basaltic rocks under cold, dry climatic conditions in Greenland formed both nontronite and well-crystalline iron oxides (goethite and magnetite/maghemite) in closed crack microenvironments due to water availability (Koch et al., 1995). The formation of jarosite in the Xiakou section is thus likely attributable to highly localized variation in porewater chemistry, pH and redox conditions.

The Xiakou section contains notably more sulfur than in P-T sequences elsewhere in South China despite lack of evidence for the presence of sulfide deposits at or near the Xiakou area. Total sulfur values are mostly 0.08-2.50% (versus 0.01-0.03% at Dongpan and 0.00-0.05% at Xinmin), suggesting locally higher sulfur inputs to Xiakou (Kump et al., 2005; Pei et al., 2020). Furthermore, all tuff beds yield higher sulfur contents than their host rocks (Shen, 2014), indicating that sulfur uptake at Xiakou was associated with volcanic ash deposition. The observation that jarosite is found only in tuffs at Xiakou and not in cogenetic volcanic ash beds in other South China P-T boundary sections—despite all of the tuffs having a shared origin in intermediate to felsic subduction-zone volcanism of the eastern Tethys (Shen et al., 2013; Yin et al., 1992)—is an indication that excess sulfur was delivered through upwelling of a H_2S-rich, euxinic deep watermass. The presence of this H_2S-rich watermass allowed sulfates including jarosite to form in freshly deposited ash beds on the Xiakou seafloor. The absence of jarosite and heavy $\delta^{34}S$ values of tuffs in the upper Xiakou profile (e.g., L259b and L271) are attributable to a reduction in upwelling intensity (Fig. 3; Table 2). The presence of jarosite in background sediments (mudstones) adjacent to tuff bed L255 can be interpreted as the product of mixing with volcanogenic ash, as reflected by the presence of I/S clays in the mudstones (Table 1).

In certain ancient and recent marine sediments, the formation of gypsum and bassanite can involve mainly alteration of volcanogenic materials with no sulfur input, especially in those having context of convergent margins or basaltic plateaus (Hoareau et al., 2011), since volcanism in this tectonic environment often links to voluminous outgassing and input of volcanic sulfate aerosols (McKenzie et al., 2016). However, formation of jarosite in various magmatic tuffs has not been observed except for limited cases in altered volcanogenic rocks around the volcanic vents due to sulfur-bearing outgassing (Zimbelman et al., 2005). This observation suggests that jarosite is unlikely to form from weathering of tuffs without the flux of sulfur during the alteration process.

At Xiakou, it is clear that flux of H_2S upwelling in association with subaqueous weathering of volcanogenic materials is the major process leading to saturation and precipitation of jarosite in sediment porewaters. The preservation of jarosite in the Xiakou sediments is most likely attributed to the acidic brine porewater, owing to the elevated salinity, anoxic, and euxinic depositional environment (Pei et al., 2020), the acidic condition due to lasting H_2S flux, and subsequently the decreasing water activity by elevated temperature and enhanced compaction in burial diagenesis. Devitrification of volcanic ash yields mainly smectitic clay minerals during early diagenesis (40° to 100 °C; Fortey et al., 1996), which will transform into I/S clays and sometimes almost pure illite in burial diagenesis due to increasing temperature (Huff, 2016). The weak activity of fluid flow during burial diagenesis also contributes to the stability of jarosite, as reflected by the presence of mainly I/S clays and absence of diagenetic mineral phases in the tuff beds. To date, jarosite formation observed in the Xiakou tuffs within the P-T strata confirms that extremely acidic conditions linked to upwelling of H_2S formed by sulfate-reducing bacteria (SRB), indicative of the microbe-induced formation of jarosite during weathering of volcanogenic materials in water.

IMPLICATIONS

Jarosite in the Xiakou P-T section exhibits striking mineralogical and morphological similarities to occurrences of jarosite in Meridiani Planum sediments, suggesting that the former is a possible analogue for Martian sulfate-bearing settings. The essential conditions for jarosite formation at Xiakou are concurrent deposition of volcanic airfall materials, a flux of oxygen (co-transported with the ash), and upwelling of H_2S from a deep euxinic watermass. Although the felsic-intermediate source rocks at Xiakou differ from the primarily basaltic source rocks on Mars, the implications for sulfate formation during subaqueous weathering of volcanogenic materials concurrent with H_2S influx are likely similar. Smectite-bearing Noachian and Hesperian-aged sedimentary rocks on Mars are analogous to altered volcanogenic materials in an open water body on Earth, since the weathering products of volcanic materials under such conditions tend to be monomineralic (Jeans et al., 2000). The Xiakou depositional environment is analogous to smectite-bearing ancient lake basins on Mars such as the Gale and Jezero craters. The limited illitisation of smectite on Mars was likely the result of low burial temperatures and a lack of K^+ in

diagenetic fluids (Borlina et al., 2015; Bristow et al., 2018), analogous to shallow lacustrine settings in Turkey in which thick bentonites have accumulated (Özdamar et al., 2014; Kadír et al., 2017).

Calcium sulfate is present as late diagenetic veins at many Mars rover landing sites, but it is also likely present in the sedimentary matrix (Vaniman et al., 2018). As in the Xiakou tuffs, some gypsum in smectite-bearing Martian mudstones can be explained as a non-evaporitic mineral, formed in a closed-basin environment through weathering of volcanogenic materials with limited influx of sulfur. Bassanite and anhydrite can further form from dehydration of gypsum during subsequent burial diagenesis due to increasing porewater temperature and salinity (Hoareau et al., 2011). In particular, sulfates including jarosite in the mudstones of the Murray formation in Gale crater occur as dispersed crystals in the fine-grained matrix or as cement in nodules, dendrites, and veins (Hurowitz et al., 2017), consistent with precipitation from porewaters during burial diagenesis (Kah et al., 2018). Moreover, the relatively young age of jarosite in a single target from the Murray formation indicates a late-diagenetic or a weathering product origin for Martian jarosite (Martin et al., 2017). This mineral assemblage is analogous to that in the Xiakou tuffs.

The presence of sulfates (including jarosite) in the Murray formation mudstones has been attributed to an influx of sulfuric acid, likely related to volcanic outgassing (Bibring et al., 2006), or to acidic groundwaters during diagenesis (Rampe et al., 2017). However, an alternative hypothesis for their origin is subaqueous weathering of volcanogenic materials in conjunction with upwelling of H_2S from below a euxinic chemocline in an open water body on the surface of Mars. Although these volcanogenic materials may have contained highly soluble volcanic sulfate aerosols, volcanic-induced acidification likely took place in a relatively short interval of time such that it did not cause widespread acid-sulfate alteration (Cronin et al., 2014; Kump et al., 2005). The extremely acidic environment could be produced due to intensive H_2S upwelling in association with the disturbance of deposition of volcanogenic materials in the basin, analogous to the jarosite formed in the Xiakou tuffs. The accumulation of H_2S in the background sediments of the basin could be possibly derived from sulfate-reducing bacteria, especially because SRB can do this faster - on biological time scales rather than geologic ones, and the upwelling of H_2S-bearing fluids may be induced due to heating from magmatic activity underlying the crater or due to dewatering of smectite during early burial diagenesis. Therefore, jarosite-bearing sediments on

Mars are potentially evidence of the former existence of microbial life on the Red Planet, which is consistent with previously reported cryptic mineralogic and organic geochemical evidence of microbial or nanobial life in Martian meteorites (Stern et al., 2022). Furthermore, bacterial sulfate reduction could explain the highly ^{34}S-depleted sulfur isotope signatures (locally to −47 ± 14‰) of sedimentary rocks from Gale crater (Franz et al., 2017; Stern et al., 2022).

REFERENCES

Algeo, T.J., Henderson, C.M., Tong, J.N., Feng, Q.L., Yin, H.F., and Tyson, R.V. (2013) Plankton and productivity during the Permian–Triassic boundary crisis: an analysis of organic carbon fluxes. Global and Planetary Change, 105, 52–67.

Bauer, A. and Velde, B. (1997) Jarosite formation in weathered siliceous chalk in Fontevrault abbey, Loire Valley, France. Mineralogical Magazine, 61, 705–711.

Benison, K.C. (2006) A Martian analog in Kansas: Comparing Martian strata with Permian acid saline lake deposits. Geology, 34, 385–388.

Bibring, J.P., Langevin, Y., Mustard, J.F., Poulet, F., Arvidson, R., Gendrin, A., Gondet, B., Mangold, N., Pinet, P., Forget, F., and the OMEGA team. (2006) Global mineralogical and aqueous Mars history derived from OMEGA/Mars express data. Science, 312, 400–404.

Borlina, C.S., Ehlmann, B.L., and Kite, E.S. (2015) Modeling the thermal and physical evolution of Mount Sharp's sedimentary rocks, Gale crater, Mars: Implications for diagenesis on the MSL Curiosity rover traverse. Journal of Geophysical Research: Planets, 120(8), 1396–1414.

Bristow, T.F., Rampe, E.B., Achilles, C.N., Blake, D.F., Chipera, S.J., Craig, P., Crisp, J.A., Des Marais, D.J., Downs, R.T., Gellert, R., Grotzinger, J.P., Gupta, S., Hazen, R.M., Horgan, B., Hogancamp, J.V., Mangold, N., Mahaffy, P.R., McAdam, A.C., Ming, D.W., Morookian, J.M., Morris, R.V., Morrison, S.M., Treiman, A.H., Vaniman, D.T., Vasavada, A.R., and Yen, A.S. (2018) Clay mineral diversity and abundance in sedimentary rocks of Gale crater, Mars. Science Advances, 4(6), eaar3330.

Chaikovskiy, II., Chaikovskaya, E.V., Korotchenkova, O.V., Chirkova, E.P., and Utkina, T.A. (2019) Authigenic titanium and zirconium minerals at the Verkhnekamskoe salt deposit. Geochemistry International, 57, 184–196.

Christidis, G.E. (1998) Comparative study of the mobility of major and trace elements during

alteration of an andesite and a rhyolite to bentonite, in the islands of Milos and Kimolos, Aegean, Greece. Clays and Clay Minerals, 46, 379–399.

Cronin, S.J., Stewart, C., Zernack, A.V., Brenna, M., Procter, J.N., Pardo, N., Christenson, B., Wilson, T., Stewart, R.B., and Irwin, M. (2014) Volcanic tuff leachate compositions and assessment of health and agricultural hazards from 2012 hydrothermal eruptions, Tongariro, New Zealand. Journal of Volcanology and Geothermal Research, 286, 233–247.

De La Fuente, S., Cuadros, J., and Linares, J. (2002) Early stages of volcanic tuff alteration in hydrothermal experiments: formation of mixed-layer illite-smectite. Clays and Clay Minerals, 50, 578–590.

Ehlmann, B.L. and Edwards, C.S. (2014) Mineralogy of the Martian surface. Annual Review of Earth and Planetary Sciences, 42, 291–315.

Elwood Madden, M.E., Madden, A.S., Rimstidt, J.D., Zahrai, S., Kendall, M.R., and Miller, M.A. (2012) Jarosite dissolution rates and nanoscale mineralogy. Geochimica et Cosmochimica Acta, 91, 306–321.

Elwood Madden, M.E., Bodnar, R.J., and Rimstidt, J.D. (2004) Jarosite as an indicator of water-limited chemical weathering on Mars. Nature, 431, 821–823.

Fortey, N.J., Merriman, R.J., and Huff, W.D. (1996) Silurian and Late-Ordovician K-bentonites as a record of late Caledonian volcanism in the British Isles. Transactions of the Royal Society of Edinburgh Earth Sciences 86, 167–180.

Franz, H.B., McAdam, A.C., Ming, D.W., Freissinet, C., Mahaffy, P.R., Eldridge, D.L., Fischer, W.W., Grotzinger, J.P., House, C.H., Hurowitz, J.A., and McLennan, S.M. (2017) Large sulfur isotope fractionations in Martian sediments at Gale crater. Nature Geoscience, 10(9), 658–662.

Fu, J., Hu, Z., Li, J., Yang, L., Zhang, W., Liu, Y., Li, Q., Zong, K., and Hu, S. (2017) Accurate determination of sulfur isotopes ($\delta^{33}S$ and $\delta^{34}S$) in sulfides and elemental sulfur by femtosecond laser ablation MC-ICP-MS with non-matrix matched calibration. Journal of Analytical Atomic Spectrometry, 32, 2341–2351.

Hoareau, G., Monnin, C., and Odonne, F. (2011) The stability of gypsum in marine sediments using the entire ODP/IODP porewater composition database. Marine Geology, 279, 87–97.

Hong, H.L., Ji, K.P., Liu, C., Algeo, T.J., Yin, K., Zhao, L.L., Hochella, M.F., Fang, Q., and Wang,

C.W. (2022) Authigenic anatase nanoparticles as a proxy for sedimentary environment and porewater pH. American Mineralogist, 107, 2176–2187.

Hong, H.L., Ji, K.P., Hei, H.T., Wang, C.W., Liu, C., Zhao, L.L., Lanson, B., Zhao, C.L., Fang, Q., and Algeo, T.J. (2023) Clay mineral evolution and formation of intermediate phases during pedogenesis on picrite basalt bedrock under temperate conditions (Yunnan, southwestern China). Catena 220, 106677.

Huff, W.D. (2016) K-bentonites: a review. American Mineralogist, 101, 43–70.

Hurowitz, J.A., Grotzinger, J.P., Fischer, W.W., McLennan, S.M., Milliken, R.E., Stein, N., Vasavada, A.R., Blake, D.F., Dehouck, E., Eigenbrode, J.L., Fairén, A.G., Frydenvang, J., Gellert, R., Grant, J.A., Gupta, S., Herkenhoff, K.E., Ming, D.W., Rampe, E.B., Schmidt, M.E., Siebach, K.L., Stack-Morgan, K., Sumner, D.Y., and Wiens, R.C. (2017) Redox stratification of an ancient lake in Gale crater, Mars. Science, 356, eaah6849.

Jeans, C.V., Wray, D.S., Merriman, R.J., and Fisher, M.J. (2000) Volcanogenic clays in Jurassic and Cretaceous strata of England and the North Sea Basin. Clay Minerals, 35, 25–55.

Kadír, S., Külah, T., Önalgíl, N., Erkoyun, H., and Elliott, W.C. (2017) Mineralogy, geochemistry, and genesis of bentonites in Miocene volcanic-sedimentary units of the Ankara-Çankiri basin, central Anatolia, Turkey. Clays and Clay Minerals, 65, 64–91.

Kah, L.C., Stack, K.M., Eigenbrode, J.L., Yingst, R.A., and Edgett, K.S. (2018) Syndepositional precipitation of calcium sulfate in Gale Crater, Mars. Terra Nova, 30, 431–439.

Kampschulte, A. and Strauss, H. (2004) The sulfur isotopic evolution of Phanerozoic seawater based on the analysis of structurally substituted sulfate in carbonates. Chemical Geology, 204(3-4), 255–286.

Kaplan, I.R. and Ritterberg, S.C. (1964) Microbiological fractionation of sulphur isotopes. Journal of General Microbiology, 34, 195–212.

Koch, C.B., Mørup, S., Madsen, M.B., and Vistisen, L. (1995) Iron-containing weathering products of basalt in a cold, dry climate. Chemical Geology, 122, 109–119.

Kump, L.R., Pavlov, A., and Arthur, M.A. (2005) Massive release of hydrogen sulfide to the surface ocean and atmosphere during intervals of oceanic anoxia. Geology, 33, 397–400.

Lei, L.D., Shen, J., Li, C., Algeo, T.J., Chen, Z.Q., Feng, Q.L., Cheng, M., Jin, C.S., and Huang, J.H. (2017) Controls on regional marine redox evolution during Permian-Triassic transition in

South China. Palaeogeography, Palaeoclimatology, Palaeoecology, 486, 17–32.

Marini, L., Moretti, R., and Accornero, M. (2011) Sulfur isotopes in magmatic-hydrothermal systems, melts, and magmas. Reviews in Mineralogy and Geochemistry, 73(1), 423–492.

Martin, P.E., Farley, K.A., Baker, M.B., Malespin, C.A., Schwenzer, S.P., Cohen, B.A., Mahaffy, P.R., McAdam, A.C., Ming, D.W., Vasconcelos, P.M., and Navarro-González, R. (2017) A two-step K-Ar experiment on Mars: Dating the diagenetic formation of jarosite from Amazonian groundwaters. Journal of Geophysical Research: Planets, 122(12), 2803–2818.

McLennan, S.M., Bell, Iii J.F., Calvin, W.M., Christensen, P.R., Clark, B.D., De Souza, P.A., Farmer, J., Farrand, W.H., Fike, D.A., Gellert, R., Ghosh, A., Glotch, T.D., Grotzinger, J.P., Hahn, B., Herkenhoff, K.E., Hurowitz, J.A., Johnson, J.R., Johnson, S.S., Jolliff, B., Klingelhöfer, G., Knoll, A.H., Learner, Z., Malin, M.C., McSween, Jr H.Y., Pocock, J., Ruff, S.W., Soderblom, L.A., Squyres, S.W., Tosca, N.J., Watters, W.A., Wyatt, M.B., and Yen, A. (2005) Provenance and diagenesis of the evaporite-bearing Burns formation, Meridiani Planum, Mars. Earth and Planetary Science Letters, 240(1), 95–121.

McCollom, T.M. and Hynek, B.M. (2005) A volcanic environment for bedrock diagenesis at Meridiani Planum on Mars. Nature, 438, 1129–1131.

McKenzie, N.R., Horton, B.K., Loomis, S.E., Stockli, D.F., Planavsky, N.J., and Lee, C.T.A. (2016) Continental arc volcanism as the principal driver of icehouse-greenhouse variability. Science, 352, 444–447.

Niles, P.B. and Michalski, J. (2009) Meridiani Planum sediments on Mars formed through weathering in massive ice deposits. Nature Geoscience, 2(3), 215–220.

Özdamar, Ş., Ece, Ö.I., Uz, B., Boylu, F., Ercan, H.Ü., and Yanik, G. (2014) Element mobility during the formation of the Uzunisa-Ordu bentonite, NE Turkey, and potential applications. Clay Minerals, 49, 609–633.

Pei, Y., Duda, J.P., and Reitner, J. (2020) Sedimentary factories and ecosystem change across the Permian–Triassic Critical Interval (P–TrCI): insights from the Xiakou area (South China). PalZ, doi: 10.1007/s12542-020-00530-x.

Potter-McIntyre, S.L. and McCollom, T.M. (2018) Jarosite and alunite in ancient terrestrial sedimentary rocks: reinterpreting Martian depositional and diagenetic environmental conditions. Life 8, 32.

Poulet, F., Bibring, J-P, Mustard, J.F., Gendrin, A., Mangold, N., Langevin, Y., Arvidson, R.E., Gondet, B., Gomez, C., and the Omega Team (2005) Phyllosilicates on Mars and implications for early Martian climate. Nature, 438, 623–27.

Rampe, E.B., Ming, D.W., Blake, D.F., Bristow, T.F., Chipera, S.J., Grotzinger, J.P., Morris, R.V., Morrison, S.M., Vaniman, D.T., Yen, A.S., Achilles, C.N., Craig, P.I., Des Marais, D.J., Downs, R.T., Farmer, J.D., Fendrich, K.V., Gellert, R., Hazen, R.M., Kah, L.C., Morookian, J.M., Peretyazhko, T.S., Sarrazin, P., Treiman, A.H., Berger, J.A., Eigenbrode, J., Fairén, A.G., Forni, O., Gupta, S., Hurowitz, J.A., Lanza, N.L., Schmidt, M.E., Siebach, K., Sutter, B., and Thompson, L.M. (2017) Mineralogy of an ancient lacustrine mudstone succession from the Murray formation, Gale crater, Mars. Earth and Planetary Science Letters, 471, 172–185.

Rampe, E.B., Blake, D.F., Bristow, T.F., Ming, D.W., Vaniman, D.T., Morris, R.V., Achilles, C.N., Chipera, S.J., Morrison, S.M., Tu, V.M., Yen, A.S., Castle, N., Downs, G.W., Downs, R.T., Grotzinger, J.P., Hazen, R.M., Treiman, A.H., Peretyazhko, T.S., Des Marais, D.J., Walroth, R.C., Craig, P.I., Crisp, J.A., Lafuente, B., Morookian, J.M., Sarrazin, P.C., Thorpe, M.T., Bridges, J.C., Edgar, L.A., Fedo, C.M., Freissinet, C., Gellert, R., Mahaffy, P.R., Newsom, H.E., Johnson, J.R., Kah, L.C., Siebach, K.L., Schieber, J., Sun, V.Z., Vasavada, A.R., Wellington, D., Wiens, R.C., and the MSL Science Team. (2020) Mineralogy and geochemistry of sedimentary rocks and eolian sediments in Gale crater, Mars: A review after six Earth years of exploration with Curiosity. Geochemistry, 80(2), https://doi.org/10.1016/j.chemer.2020.125605.

Reynolds Jr., R.C., Reynolds III, R.C., 1996. NEWMOD-for-Windows. The Calculation of One-dimensional X-ray Diffraction Patterns of Mixed-layered Clay Minerals. Hanover, New Hampshire.

Saricaoglu, S., Dengiz, O., and Isik, K. (2021) Assessment of biogeochemical-mineralogical characteristic and weathering indices of soils developed on basaltic parent material and toposequence under subhumid ecosystem. Geomicrobiology Journal 38, 451–465.

Shen, J. (2014) Volcanic Effects to Marine Environments and Organisms across the Permian–Triassic transition in South China. *Ph.D. Thesis*. China University of Geosciences (Wuhan).

Shen, J., Algeo, T.J., Feng, Q., Zhou, L., Feng, L., Zhang, N., and Huang, J. (2013) Volcanically induced environmental change at the Permian–Triassic boundary (Xiakou, Hubei Province,

This is the peer-reviewed, final accepted version for American Mineralogist, published by the Mineralogical Society of America.
The published version is subject to change. Cite as Authors (Year) Title. American Mineralogist, in press.
DOI: https://doi.org/10.2138/am-2023-9062. http://www.minsocam.org/

South China): related to West Siberian coal-field methane releases? Journal of Asian Earth Sciences, 75, 95–109.

Somelar, P., Kirsimäe, K., Hints, R., and Kirs, J. (2010) Illitization of early Paleozoic K-bentonites in the Baltic basin: Decoupling of burial- and fluid-driven processes. Clays and Clay Minerals, 58, 388–398.

Środoń, J., Drits, V.A., McCarty, D.K., Hsieh, J.C.C., and Eberl, D.D. (2001) Quantitative X-ray diffraction analysis of clay-bearing rocks from random preparations. Clays and Clay Minerals, 49, 514–528.

Stern, J.C., Malespin, C.A., Eigenbrode, J.L., Webster, C.R., Flesch, G., Franz, H.B., Graham, H.V., House, C.H., Sutter, B., Archer, P.D., and Jr Hofmann, A.E. (2022) Organic carbon concentrations in 3.5-billion-year-old lacustrine mudstones of Mars. Proceedings of the National Academy of Sciences (U.S.A.), 119(27), e2201139119.

Sulieman, M.M., Sh Sallam, A., Brevik, E.C., and Al-farraj, A.S. (2020) Investigation of the clay minerals composition of soils derived from basalt parent materials in the Early Miocene to Early Pleistocene on the Arabian Shield using multiple techniques: implications for paleoclimatic conditions. Environmental Earth Sciences 79, 297.

Vaniman, D.T., Martínez, G.M., Rampe, E.B., Bristow, T.F., Blake, D.F., Yen, A.S., Ming, D.W., Rapin, W., Meslin, P.Y., Morookian, J.M., Downs, R.T., Chipera, S.J., Morris, R.V., Morrison, S.M., Treiman, A.H., Achilles, C.N., Robertson, K., Grotzinger, J.P., Hazen, R.M., Wiens, R.C., and Sumner, D.Y. (2018) Gypsum, bassanite, and anhydrite at Gale crater, Mars. American Mineralogist, 103, 1011–1020.

Yin, H.F., Huang, S.J., Zhang, K.X., Hansen, H.J., Yang, F.Q., Ding, M.H., and Bie, X.M. (1992) The effects of volcanism on the Permo-Triassic mass extinction in South China. In: Sweet, W.C., Yang, Z., Dickins, J.M., Yin, H. (Eds.). *Permo-Triassic Events in the Eastern Tethys*. Cambridge University Press, Cambridge, 169–174.

Yoshida, H., Hasegawa, H., Katsuta, N., Maruyama, I., Sirono, S., Minami, M., Asahara, Y., Nishimoto, S., Yamaguchi, Y., Ichinnorov, N., and Metcalfe, R. (2018) Fe-oxide concretions formed by interacting carbonate and acidic waters on Earth and Mars. Science Advances, 4, eaau0872.

Zimbelman, D.R., Rye, R.O., and Breit, B.N. (2005) Origin of secondary sulfate minerals on

Always consult and cite the final, published document. See http:/www.minsocam.org or GeoscienceWorld

This is the peer-reviewed, final accepted version for American Mineralogist, published by the Mineralogical Society of America.
The published version is subject to change. Cite as Authors (Year) Title. American Mineralogist, in press.
DOI: https://doi.org/10.2138/am-2023-9062. http://www.minsocam.org/

active andesitic stratovolcanoes. Chemical Geology, 215, 37– 60.

Zolotov, M.Y. and Shock, E.L. (2005) Formation of jarosite-bearing deposits through aqueous oxidation of pyrite at Meridiani Planum, Mars. Geophysical Research Letters, 32, L21203, doi:10.1029/2005GL024253.

Acknowledgments:

We wish to thank Dr. Y.J.L., Q.F., K.Y., and J.Z. for their assistance in HRTEM and SEM analyses, and especially thank Prof. Lindsay McHenry, the handling editor, and Dr. Sally Potter-McIntyre for their insightful reviews, valuable comments, and suggestions. **Funding**: This work was supported by the Natural Science Foundation of China [42172045, 41972040]. **Author contributions**: H.L.H. conceived, designed, and performed the research and wrote the original draft. C.L. performed the XRD, SEM, and HRTEM analyses. T.J.A. and R.E.B. wrote some paragraphs and edited the paper. **Conflict of Interest**: Conflict of interest statement. None declared. **Data and materials availability**: All raw data and results including the images in Gatan DM ImageDocument format are available when request.

Supplementary Materials

Fig S1 to S2

Table S1 to S4

Always consult and cite the final, published document. See http:/www.minsocam.org or GeoscienceWorld

This is the peer-reviewed, final accepted version for American Mineralogist, published by the Mineralogical Society of America.
The published version is subject to change. Cite as Authors (Year) Title. American Mineralogist, in press.
DOI: https://doi.org/10.2138/am-2023-9062. http://www.minsocam.org/

Table 1 Relative proportions of clay species of clay fraction from the Xiakou sediments (wt%)

Sample	Lithology	Illite	Chlorite	Kaolinite	I/S clays
L278	Mudstone	94±3	6±1	/	/
L277	Tuff	/	/	/	100
L276	Mudstone	84±2	16±2	/	/
L272	Marl	73±3	28±2	/	/
L271	Tuff	/	/	6±1	94±7
L270	Marl	97±4	3±1	/	/
L268	Mudstone	97±5	3±1	/	/
L267b	Tuff	40±3	7±1	/	53±6
L267a	Mudstone	90±3	10±2	/	/
L266a	Mudstone	98±3	2±1	/	/
L266	Tuff	/	/	/	100
L265b	Mudstone	96±3	4±1	/	/
L265a	Mudstone	95±6	5±1	/	/
L264	Tuff	3±1	/	/	97±5
L263	Mudstone	98±3	2±1	/	/
L261a	Marl	97±5	3±1	/	/
L261	Mudstone	76±3	11±2	/	13±2
L260	Tuff	/	/	/	100
L259b	Tuff	/	/	/	100
L259a	Marl	75±2	5±1	/	20±3
L256	Mudstone	69±3	3±1	/	28±2
L255	Tuff	/	/	/	100
L254	Mudstone	76±2	9±1	/	15±2

Always consult and cite the final, published document. See http:/www.minsocam.org or GeoscienceWorld

This is the peer-reviewed, final accepted version for American Mineralogist, published by the Mineralogical Society of America.
The published version is subject to change. Cite as Authors (Year) Title. American Mineralogist, in press.
DOI: https://doi.org/10.2138/am-2023-9062. http://www.minsocam.org/

Table 2 Mineral and sulfur isotopic compositions of the Xiakou sediments

Sample	Lithology	Dolomite	Ankerite	Calcite	Pyrite	Jarosite	Bassanite	Gypsum	Quartz	Plagioclase	K-feldspar	Clay minerals	K_2O	$^{34}S_{CaSO4}$	$^{34}S_{pyrite}$
L278	Mudstone	2	16	1	2	/	/	/	17	2	/	60	2.69	/	–15.96
L277	Tuff	/	/	/	/	1	1	1	1	/	/	96	6.07	–6.62±1.36	/
L276	Mudstone	3	16	5	2	/	/	/	20	3	/	51	2.76	/	+2.07
L272	Mudstone	1	39	7	4	/	/	/	18	/	/	31	1.30	/	+2.87
L271	Tuff	/	/	1	/	/	/	/	1	/	/	98	6.18	/	–15.28
L270	Mudstone	1	6	46	/	/	/	/	10	2	/	35	0.89	/	–6.59
L269	Marl	1	13	3	2	1	/	/	24	8	/	48	3.67	/	–29.89
L267b	Tuff	/	/	/	1	3	4	/	26	7	/	59	4.49	+3.20±1.23	–29.01
L267a	Mudstone	2	20	1	4	/	/	/	17	3	/	53	2.73	/	–39.85
L266a	Mudstone	2	/	/	/	/	/	/	24	4	/	70	0.95	/	+33.74
L266	Tuff	/	/	/	1	4	/	1	1	1	/	92	5.38	–37.23 ±0.71	–25.96
L265b	Mudstone	/	21	/	3	/	/	1	20	2	/	53	4.33	–36.22±1.54	–25.73
L265a	Mudstone	/	6	/	2	/	/	/	19	8	/	65	3.75	/	–34.20
L264	Tuff	/	/	/	/	6	/	1	5	/	/	88	5.32	–33.44±2.28	–34.95
L263	Mudstone	1	34	/	3	/	/	1	19	3	/	39	1.95	–35.18±0.83	–26.62
L261a	Mudstone	3	34	2	1	/	/	2	12	1	/	45	2.63	–28.36±2.40	+1.53
L261	Mudstone	1	24	1	5	/	/	/	19	3	/	47	1.00	/	+5.57
L260	Tuff	/	1	/	/	3	/	2	1	/	/	93	5.76	–29.60 ±1.67	–4.21
L259b	Tuff	/	2	3	2	/	2	/	14	2	/	75	4.91	–28.90±1.42	/
L259a	Marl	2	23	10	3	/	/	/	28	/	1	33	1.72	/	–6.29
L256	Mudstone	/	/	/	/	5	/	2	9	2	/	82	4.85	–34.46±1.29	–23.19
L255	Tuff	/	/	1	/	2	1	/	3	3	/	90	5.57	–29.86±3.94	/
L254	Mudstone	/	/	19	/	4	/	8	26	2	8	33	1.95	–21.80±2.78	–23.73

Always consult and cite the final, published document. See http:/www.minsocam.org or GeoscienceWorld

This is the peer-reviewed, final accepted version for American Mineralogist, published by the Mineralogical Society of America.
The published version is subject to change. Cite as Authors (Year) Title. American Mineralogist, in press.
DOI: https://doi.org/10.2138/am-2023-9062. http://www.minsocam.org/

Note: Mineral and sulfur contents in wt% and $\delta^{34}S$ values in ‰, the relative error of mineral contents is <15%; $\delta^{34}S_{pyrite}$ from Shen et al. (2013); and "/" is under detection limit.

Always consult and cite the final, published document. See http:/www.minsocam.org or GeoscienceWorld

This is the peer-reviewed, final accepted version for American Mineralogist, published by the Mineralogical Society of America.
The published version is subject to change. Cite as Authors (Year) Title. American Mineralogist, in press.
DOI: https://doi.org/10.2138/am-2023-9062. http://www.minsocam.org/

Table 3 The zoned distribution of $\delta^{34}S$ value of gypsum showing the evolution of porewater with diagenesis

Sample	Lithology	Jarosite	Bassanite	Gypsum	K_2O	$^{34}S_{CaSO4}$(‰)	Zoned grains (center to margin); $^{34}S_{CaSO4}$ (‰) (errors in accuracy < 0.7‰)
L277	Tuff	0.66	0.87	0.31	6.07	-6.62±1.36	-7.88, -6.34, -4.16, -3.28, -3.55, -3.71, -0.18, -0.39
L266	Tuff	3.93	/	0.41	5.38	-37.23±0.71	-37.80, -35.74
L261a	Mudstone	/	/	2.40	2.63	–28.36±2.40	-24.24, -28.19
L255	Tuff	2.46	0.90	/	5.57	-29.86±3.94	-30.74, -24.88, -19.38 (Grain #1) -28.94, 20.56 (Grain #2)
L254	Mudstone	4.32	/	7.79	1.95	-21.80±2.78	-15.12, -20.11

Always consult and cite the final, published document. See http:/www.minsocam.org or GeoscienceWorld